CrossMark
click for updates

Silver nanoparticles supported on zirconia–ceria for the catalytic wet air oxidation of methyl *tert*-butyl ether

Z. Guerra-Que,[a] G. Torres-Torres,[a] H. Pérez-Vidal,*[a] I. Cuauhtémoc-López,[a] A. Espinosa de los Monteros,[a] Jorge N. Beltramini[b] and D. M. Frías-Márquez[c]

In this work Ag nanoparticles supported on ZrO_2–CeO_2 promoted with different amounts of CeO_2 (0, 0.5, 1, 5, 10, 15 and 20 wt%) were synthesized by deposition–precipitation method in order to test the Catalytic Wet Air Oxidation (CWAO) of Methyl *Tert*-Butyl Ether (MTBE). X-ray diffraction patterns reveal that the tetragonal ZrO_2 phase (t-ZrO_2) present in the catalysts is stabilized by the presence of CeO_2, forming a solid solution, and preventing transformation to the monoclinic phase (m-ZrO_2). The t-ZrO_2 stability and the dispersion of Ag on ZrO_2 increase with CeO_2 concentration. HRTEM images confirmed that the mean crystallite size of supports and monometallic Ag catalyst decreases by CeO_2 addition. CeO_2 can also improve the reduction of Ag_2O and increase also the d-electron density of the surface silver atoms. Furthermore, CeO_2 has a promoting effect on silver supported zirconia–ceria because of the strong metal–support interaction and its relationship of oxygen vacancies of zirconia–ceria support. The extent of reduction of silver controls the quantity of oxygen to be adsorbed during the catalytic oxidation reaction. In general, a small crystal size and high metallic dispersion can enhance the activity of MTBE catalytic wet air oxidation. The Ag/ZrO_2–(15%)CeO_2 catalyst was the most active with 90% MTBE conversion.

Introduction

At present, concern about the treatment of generated pollutants discarded into the groundwater has increased in world chemical industries such as petrochemicals. This wastewater can present a potentially harmful impact on both the environment and humans, when quantities exceed the limits permitted per day and even more if they are untreated or the treatment is inadequate.[1–3] The composition and concentration of wastewater depend on operating conditions of the industrial process but they certainly contain both organic matter and toxic pollutants of different molecular weights. Contaminants can be simple such as acetic acid or complex such as polymers. Within the group of organic pollutants, there are those called refractories, characterized for being non-biodegradable, remaining in a certain concentration even in treated water and for being highly toxic, hence its importance.[4] Conventional physicochemical methods are inefficient for the treatment of effluents containing this type of compounds, as they do not destroy them completely and this can result in even more toxic intermediates than the initial compounds. Biological treatment has been used as an alternative, which is an economical method to treat this type of wastewater.[5,6] Lot of bacteria have been reported to treat organic contaminants dissolved in waste effluents, however in some cases as in wastewater from oil industry it has not shown the desired effectiveness, because this wastewater has a high content of NaCl, and this directly affects the microorganisms responsible of the treatment, inhibiting microbial growth.[1,4,7] Within refractory organic molecules there is the Methyl *Tert*-Butyl Ether (MTBE). MTBE is used as an octane gasoline enhancer additive that is presumably important for reducing air pollution by decreasing carbon monoxide emanating from car exhausts. Unfortunately, this additive has been found present in groundwater and surface water due to leakages from car or underground fuel tanks creating a serious environmental problem due to its refractory properties to degrade when releases into the environment.[8–11]

In search of a suitable and efficient method to degrade MTBE, there have been many applications of advanced oxidation processes with very promising results. Within this technology is found the Catalytic Wet Air Oxidation (CWAO).[12–17]

CWAO it is regarded one of the most important industrial processes to destroy hazardous, toxic and non-biodegradable

[a]Universidad Juárez Autónoma de Tabasco, Laboratorio de Catálisis Heterogénea, Área de Química, DACB, Km. 1 Carretera Cunduacán-Jalpa de Méndez A.P. 24, Cunduacán, C.P. 86690, Tabasco, Mexico. E-mail: hermicenda.perez@ujat.mx; Fax: +52 19143360928; Tel: +52 19143360300

[b]ARC Centre of Excellence for Functional Nanomaterials, The Australian Institute for Bioengineering and Nanotechnology, School of Engineering, The University of Queensland, St. Lucia, QLD 4072, Australia

[c]Universidad Juárez Autónoma de Tabasco, DAIA, Km. 1 Carretera Cunduacán-Jalpa de Méndez, Col. La Esmeralda, Cunduacán, C.P. 86690, Tabasco, Mexico

organic compounds present in wastewater streams. The process involves the use of a tickle-bed or slurry reactors operating at temperatures in the range of 100–325 °C at 5–200 bar pressures, with oxygen as oxidant agent.[14–16,18,19]

For long catalytic oxidation reactions have shown a positive effect controlling and decreasing the pollutant concentration found in air and water sources. On this regard, silver supported catalysts have shown an excellent behavior for this reaction. Silver as a metal noble has special features to improve catalytic oxidation reactions. It is known silver can chemisorb O_2;[20] silver can also catalyze CO oxidation, although at higher temperatures than gold.[21,22] Studies on selective catalytic reduction (SCR) of C_3H_6 over Ag/Al_2O_3 catalyst has shown that not only the silver content is important but also the presence of different AgO species as a result of pretreatment with O_2 at 500 °C are essential for the selective reduction and improved conversion of C_3H_6.[23] Similar behavior was reported by Zhenping et al.[24] Oxygen chemisorption on silver surface as a pretreatment generates various oxygen species such as bulk-oxygen (O_β) and subsurface oxygen (O_γ), which are responsible of the higher catalytic activity in hydrocarbon, formaldehyde (methanal) and soot oxidation.[24–26] On the other hand, ceria with its ability to store and release oxygen, plays an important role in catalysis, participating directly in the conversion of environmentally sensitive molecules such as phenol and acetic acid into carbon dioxide, water and/or intermediate products. Ceria as a support has oxygen storage capacity (OSR) and redox properties. Oxygen reducibility and oxygen storage capacity seem to be important properties for the performance of ceria in oxidation reactions.[27] These properties originated from its easy creation and diffusion of oxygen vacancies, especially at the support surface level. It was established that the extraction of an oxygen vacancy is associated with a reduction of Ce(IV) species to Ce(III).[28,29] Then the lattice of ceria compensates the anion vacancy with this charge conversion enhancing its catalytic oxidation properties. Rare earth metals and transition metals were also frequently employed for this purpose.[30,31] Another important factor is played by the diffusion rate of oxygen; consequently, it is important to enhance this property. It was also found that the tetragonal phase of zirconia oxide that is thermally stable at high temperatures plays an important role on oxidation reactions due to its high oxygen ion conductivity properties.[26,32] The critical step in the effective development of CWAO is the preparation of an efficient and durable catalyst. Therefore, this paper deals with the study of the catalytic properties of Ag supported on ZrO_2–CeO_2 for the catalytic wet oxidation degradation of MTBE using a batch reactor unit. The synergistic effect of metal and support on the reaction is also reported.

Experimental

Supports preparation

The zirconia (ZrO_2) and zirconia (ZrO_2–CeO_2) supports were prepared by the sol gel method. The ZrO_2 support was prepared using zirconia n-butoxide (Aldrich) as precursor. A mixture of n-butanol–water was stirred and kept in reflux at 80 °C. Zirconia n-butoxide was added drop by drop for 3 hours to this solution

until a gel was formed. The mixture was constantly stirred for 24 hours at 80 °C. After the water and alcohol remaining were eliminated by the use of a Rotavapor unit. Then the powder obtained was left in an oven to dry at 120 °C for 12 hours. The samples were calcined at 500 °C for 12 hours with heating ramp of 4 °C minute^{-1}.

The ZrO_2–CeO_2 supports were obtained by using cerium nitrate precursor salt (from Aldrich). Cerium aqueous solutions were obtained by the stoichiometric addition of precursor to obtain 0.5, 1, 5, 10, 15 and 20 wt% CeO_2. For ZrO_2–CeO_2 the same methodology used to obtain the ZrO_2 without cerium was followed and the precursor salt was added to then-butanol–water mixture before adding it to the solution of zirconia n-butoxide–water.

Catalyst preparation

The Ag supported catalysts were prepared by deposition–precipitation method (DP) of ZrO_2 and ZrO_2–CeO_2 supports adding the appropriated amounts of an aqueous solution containing silver nitrate ($AgNO_3$) to obtain a nominal concentration of 1.4% of Ag. First ZrO_2 and ZrO_2–CeO_2 support was wetted by distilled water in a beaker in order to have high dispersion and to maximize the mass transfer of added metal salt ($AgNO_3$, Baker, 99.8%) on the surface and the pores of the catalyst. Subsequently, NaOH was added drop wise to the resulting solution under constant stirring to get a pH of 10. The samples were dried at 120 °C for 12 hours and then calcined under air flow (60 ml min^{-1}) at 300 °C for 4 h, with a heat rate of 2 °C min^{-1}. Finally, the catalysts were reduced under H_2 (60 ml min^{-1}) at 400 °C for 4 h, with a heat rate of 2 °C min^{-1}.

Characterization

BET specific surface area. The surface areas of the samples were determined from the nitrogen adsorption isotherms at −196 °C using a Micromeritics Tristar 3020 II. Prior to the analysis, the samples were outgassed at 400 °C for 4 h. The adsorption data were analyzed using the ASAP 3020 software based on the Brunauer–Emmett–Teller (BET) isotherm.

X-ray diffraction (XRD). X-ray diffraction (XRD) was carried out using Rigaku Miniflex diffractometer employing Co Kα radiation ($\lambda = 0.179$ nm) obtained at 30 kV and 15 mA source with a scan speed of 2θ min^{-1}. The average crystallite size of oxide catalyst was estimated using the Scherrer equation:

$$D = \frac{0.90\lambda}{\beta \cos \theta}$$

where D is the crystallite size (nm), λ is the wavelength (nm), β is the corrected full width at half maximum (radian) and θ is the Bragg angle (radian).

DR UV-Vis spectroscopy. Diffuse reflectance UV-Vis spectra in the 900–200 nm range were obtained with a VARIAN 3000 spectrophotometer operating at room temperature.

Temperature programmed desorption under H_2 atmosphere (H_2-TPD). H_2-TPD experiments were conducted on a BELCAT equipment with thermal conductivity detector, using 0.2 g of catalyst. First the samples were pretreated with the following

protocol: 20% O_2/H_2 for 30 min at 400 °C, 20% O_2/H_2 for 1 min at 35 °C, He for 60 min at 35 °C, 5% H_2/Ar for 30 min at 400 °C, 5% H_2/Ar for 1 min at 35 °C with a flow rate of 50 sccm. Then the samples were treated by Ar at 50 sccm. The temperature was raised from room temperature to 400 °C at a heating rate of 10 °C min^{-1}. Dispersion was calculated according to mmol g^{-1} of H_2 adsorbed on each sample, metal content of silver (1.4%) and 1 : 1 Ag : H_2 stoichiometry.

Hydrogen pulse chemisorption. Hydrogen pulse chemisorption was also conducted on the BELCAT equipment. Typically, 0.1 g of catalyst was reduced at 50 °C in a flow of H_2 for 10 min and degassed with Ar at 50 °C for 10 min. Hydrogen uptake was then measured at 50 °C by injecting pulses of 5% $H_2/$Ar. The Ag dispersion was calculated based on 1 : 1 Ag : H_2 stoichiometry.

Transmission electron microscopy (TEM). Transmission electron microscopy (TEM) was performed in a JEOL JEM2100 STEM. Equipped with a JEOL JED2300 Energy Dispersive X-ray Analyzer (EDXS). The samples were ground, suspended in ethanol at room temperature, and dispersed with agitation in an ultrasonic bath for 15 min, then an aliquot of the solution was passed through a carbon copper grid.

X-ray photoelectron spectroscopy (XPS). Data was acquired using a Kratos Axis ULTRA X-ray Photoelectron Spectrometer incorporating a 165 mm hemispherical electron energy analyzer. The incident radiation was monochromatic AlKα X-rays (1486.6 eV) at 225 W (15 kV, 15 mA). Survey (wide) scans were taken at analyzer pass energy of 160 eV and multiplex (narrow) high resolution scans at 20 eV. Survey scans were carried out over 1200–0 eV binding energy range with 1.0 eV steps and a dwell time of 100 ms. Narrow high-resolution scans were run with 0.05 eV steps and 250 ms dwell time. Base pressure in the analysis chamber was 1.0×10^{-9} torr and during sample analysis 1.0×10^{-8} torr. Atomic concentrations were calculated using the CasaXPS version 2.3.14 software and a Shirley baseline with Kratios library Relative Sensitivity Factors (RSFs). Peak fitting of the high-resolution data was also carried out using the CasaXPS software.

Activity tests

All catalysts were tested in a high pressure stainless steel batch reactor (Parr Instruments) equipped with sampling valve, magnetic driven stirrer, gas supply system and temperature controller. The catalytic wet air oxidation reaction was carried out as follows: using a reaction volume of 300 ml of an aqueous solution with a concentration of 440 ppm and 1 g L^{-1} of monometallic catalyst. After the reactor was heated at 80 °C to reach the desirable temperature, pure oxygen (O_2) was added under stirring. The catalysts were previously reduced at 400 °C during 3 h with a H_2 flow (60 ml min^{-1}). The reaction was performed for 60 min. The samples in the effluent were taken at intervals of 10 min through 1 h, and the MTBE content (C), intermediate content and Total Organic Carbon (TOC) were analyzed. MTBE content and intermediate content were measured with High Performance Liquid Chromatograph (HPLC). Total Organic Carbon (TOC) of the samples was

measured with a TOC 5000 Shimadzu Analyzer. MTBE conversion and TOC was calculated using:

$$X_{MTBE} = \frac{C_0 - C_{60}}{C_0} \times 100\%$$

$$X_{TOC} = \frac{TOC_0 - TOC_{60}}{TOC_0} \times 100\%$$

where TOC_0 is total organic carbon at $t = 0$ (ppm), C_0 is the MTBE concentration at $t = 0$ (ppm), C_{60} is the MTBE concentration at $t = 1$ h of reaction (ppm), TOC_{60} is total organic carbon at $t = 1$ h of reaction (ppm). So the selectivity was calculated according to follow equation.[33]

$$S_{CO_2} = \frac{X_{TOC}}{X_{MTBE}} \times 100$$

The initial rate (r_i) was calculated from the MTBE conversion as a function of time, using the follow equation:

$$r_i = \left(\frac{\Delta_{MTBE} \ (\%)}{\Delta t m_{cat}} \right) [\text{pollutant}]_i$$

where $\frac{\Delta_{MTBE} \ (\%)}{\Delta t}$ is the conversion at initial time; $[\text{pollutant}]_i =$ initial concentration of the pollutant and $m_{cat} =$ mass of catalyst (g_{cat} L^{-1}).

Results and discussion

Catalyst characterization

Table 1 list the BET surface area of the monometallic Ag catalysts and supports. BET surface areas of the supports were found to be between 45 m^2 g^{-1} and 66 m^2 g^{-1}, while BET surface areas of the monometallic catalysts were between 46 m^2 g^{-1} and 63 m^2 g^{-1} respectively. From the results it can be seen a slight decrease of the specific surface area for the monometallic catalyst. This behavior can be explained as the micropores of the support can be plugged by the silver metal nanoparticle during synthesis causing the reduction of the surface area of monometallic catalyst. However, Ag/ZrO$_2$ catalyst showed similar surface area (46 m^2 g^{-1}) than pure ZrO$_2$ support (45 m^2 g^{-1}).[34–37]

The N$_2$ adsorption–desorption isotherms of the samples were shown in Fig. 1. Similar type IV adsorption–desorption isotherms with evident hysteresis looped at higher relative pressure (P/P_o) were observed for all samples, indicating the characteristic of mesoporous materials with ink bottle pores, as defined by IUPAC.[38–40] As also observed, hysteresis indicates the presence of capillary condensation suggesting the presence of high-strength agglomerates (aggregates).[41]

In Table 1, the dispersion of monometallic Ag catalyst determined by hydrogen pulse chemisorption and temperature programmed desorption under H_2 atmosphere is reported. It can be seen when the particle size of Ag metal decreases, the metallic dispersion increases. Besides, the dispersion of Ag was enhanced as ceria content increases. In the case of Ag/ZrO$_2$–(15%)CeO$_2$ and Ag/ZrO$_2$–(20%)CeO$_2$ the calculated dispersion is

Table 1 Physical properties of zirconia–ceria supported Ag catalyst. Average particle diameter (d_p) and metallic dispersion (D)

Support	Surface area ($m^2 g^{-1}$)	Catalyst	Surface area ($m^2 g^{-1}$)	$d_p{}^a$ (nm)	$D^{a,b}$ (%)
ZrO_2	45	Ag/ZrO_2	46	2.71	43%[a]
ZrO_2–(0.5%)CeO_2	46	Ag/ZrO_2–(0.5%)CeO_2	43	3.14	38%[a]
ZrO_2–(1%)CeO_2	43	Ag/ZrO_2–(1%)CeO_2	41	4	29%[a]
ZrO_2–(5%)CeO_2	44	Ag/ZrO_2–(5%)CeO_2	37	4.2	28%[a]
ZrO_2–(10%)CeO_2	46	Ag/ZrO_2–(10%)CeO_2	41	4.2	28%[b]
ZrO_2–(15%)CeO_2	45	Ag/ZrO_2–(15%)CeO_2	45	1.9	61%[b]
ZrO_2–(20%)CeO_2	66	Ag/ZrO_2–(20%)CeO_2	63	2.4	49%[b]

[a] Dispersion and particle diameter by hydrogen pulse chemisorption. [b] Dispersion by hydrogen temperature programmed desorption.

higher when compared with Ag/ZrO_2 catalyst. This finding was associated with the metal–support interaction effect.[27,42–44] The stabilization of Ag on ZrO_2–CeO_2 can be related to well-known phenomenon of re-dispersion of Pt on CeO_2 where the oxygen vacancy of CeO_2 plays an important role dispersing Ag into nanoparticle.[45]

Fig. 2 shows the XRD spectra of the ZrO_2, ZrO_2–(5%)CeO_2, ZrO_2–(20%)CeO_2 as well as the monometallic catalyst Ag/ZrO_2, Ag/ZrO_2–(5%)CeO_2, Ag/ZrO_2–(20%)CeO_2. Previously cubic, tetragonal and monoclinic structures have been reported for zirconia and zirconia–ceria solid solutions.[46–57] It is known that
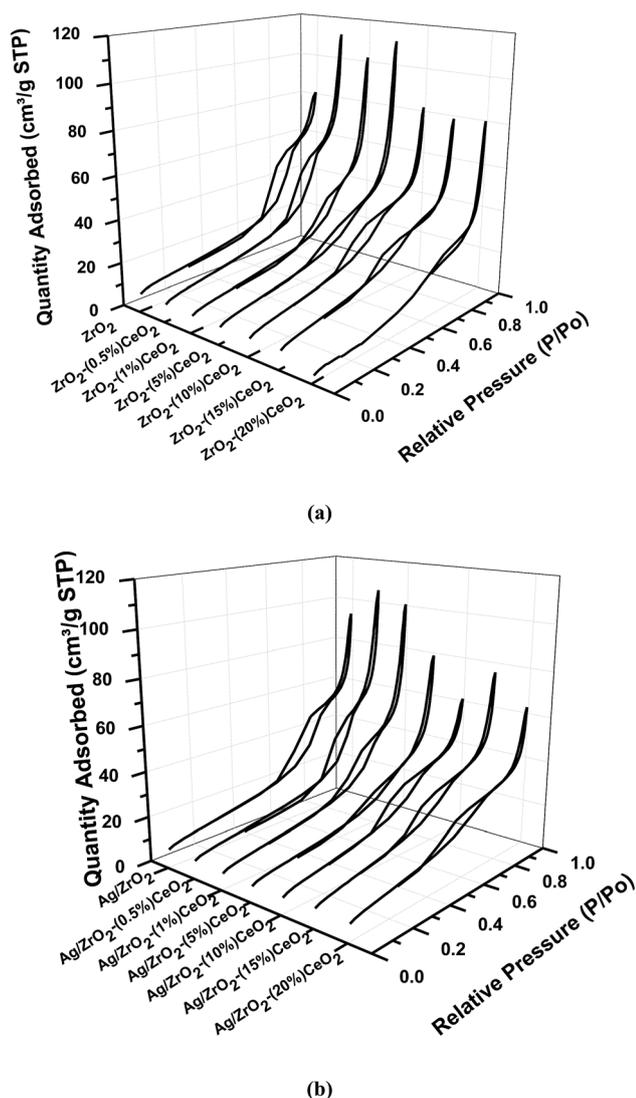

(a)

(b)

Fig. 1 Adsorption/desorption isotherms for (a) ZrO_2, ZrO_2–(X%)CeO_2 supports and (b) Ag/ZrO_2, Ag/ZrO_2–(X%)CeO_2 catalysts.

(a)

(b)
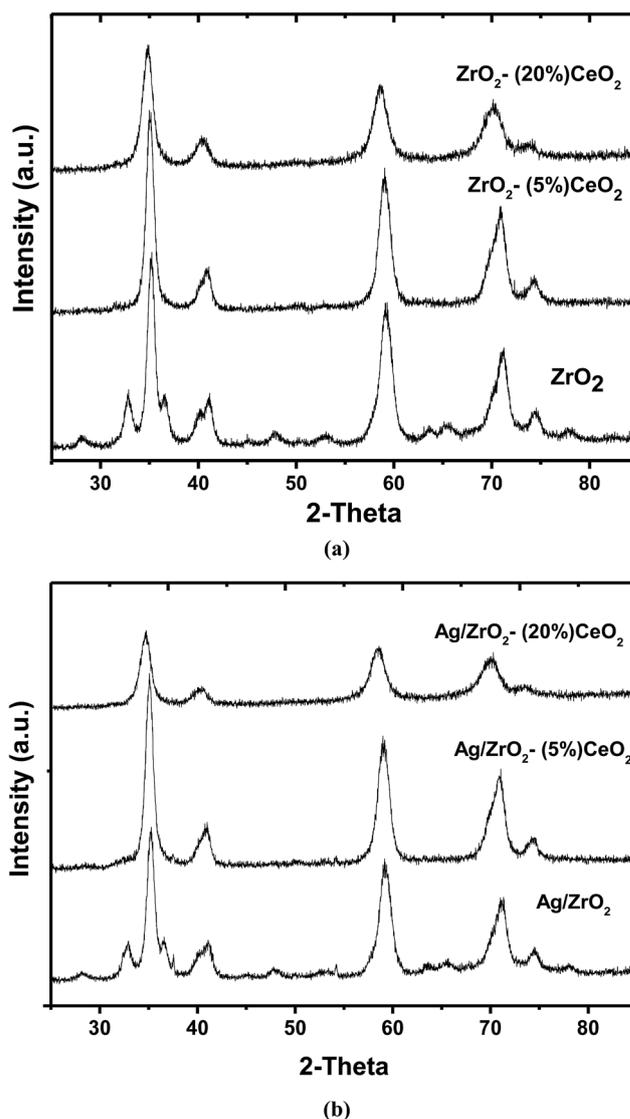
Fig. 2 X-ray diffraction patterns for (a) ZrO_2, ZrO_2–(X%)CeO_2 supports and (b) Ag/ZrO_2, Ag/ZrO_2–(X%)CeO_2 catalysts.

the crystal structures of zirconia–ceria solid solutions and their structural parameters strongly depend on its chemical composition and the synthesis method.[45,47,49,56] The XRD pattern of the prepared catalysts pure ZrO_2 and mixed ZrO_2–CeO_2 oxides calcined at 500 °C are illustrated in Fig. 2a. Four intense peaks were found at $2\theta = 35°$, $41°$, $59°$, and $71°$, which corresponds with the (111), (200), (220), and (311) planes, respectively in supports and monometallic catalysts. Pure ZrO_2 catalyst displayed the XRD pattern corresponding to the monoclinic phase with weak bands at about $33°$ and $37°$ as well as tetragonal with the main peak at $2\theta = 35°$.[46–48,51] The XRD pattern of mixed oxides catalysts is similar to that of pure ZrO_2 and no additional peaks attributed cubic CeO_2 were observed, besides, monoclinic peaks of ZrO_2 were vanished, indicating that CeO_2 was incorporated into the ZrO_2 lattice to form solid solution and sustaining the tetragonal phase.[46,48,54,57–59] The most intense lines were shifted to smaller diffraction angles with increasing CeO_2 content. This observation was attributed to expansion of the lattice due to the replacement of Zr^{4+} (ionic radius 0.084 nm) with a bigger Ce^{4+} (ionic radius 0.097 nm).[46,47,49,52–57] Solinas et al.[52] studied the effect of CeO_2 addition of ZrO_2 properties by XRD and found that the addition of CeO_2 ($\leq 25\%$) cause the formation of tetragonal structure. It is possible then pure ZrO_2 is represented by a mixture of the monoclinic and tetragonal phases. Then on zirconia–ceria supports a tetragonal phase is most likely to be found than for pure ZrO_2 supports. It indicated that the crystal phase remarkably changed with CeO_2 added to ZrO_2. Khaodee et al.,[47] explained the replacement of Zr^{4+} with larger cation such as Ce^{4+} could led to an increase of lattice defects.

The crystal size obtained using the Scherrer's equation (Table 2), shows that when smaller width of the peak, there is larger crystal size and vice versa. As a result, larger crystal size for ZrO_2 (9.7 nm) and crystal size for ZrO_2–(20%)CeO_2 (7.5 nm) were found. So here it is demonstrated that addition of dopant ceria at high content (20%) improved crystal growth. As a result, the sintering properties of zirconia can be modified by doping. The support zirconia–ceria is an excellent via for the formation of a mixed oxide since it generates excellent structural properties as reflected by the addition of ceria modified crystal growth.

The crystallites sizes of the mixed oxides decreased with increasing Ce content. The observation is in accordance with the BET surface area results shown in Table 1, where ZrO_2–CeO_2 catalysts with higher Ce loading showed larger surface area than pure ZrO_2 catalyst.

The XRD patterns of monometallic silver catalyst are presented in Fig. 2b. The introduction of 1.4% wt Ag did not change

the crystalline structure of ZrO_2 and ZrO_2–CeO_2 supports. In addition, weak diffraction peaks of the metallic Ag were observed in almost all samples, because of the intensity of these peaks were higher on the Ag/ZrO_2 samples than on the Ag/ZrO_2–($X\%$)CeO_2 catalysts; suggesting that CeO_2 dopant promote the dispersion of Ag and make its crystallite size smaller. These transformations were all beneficial to the catalytic activity.

The UV-spectra of ZrO_2 and several ZrO_2–($X\%$)CeO_2 mixed oxides prepared by sol gel method are given in Fig. 3. It can be seen several absorption bands in the UV region between 200 and 400 nm for the supports; however, for the monometallic Ag catalyst the absorption bands are in the region between 200 nm and 600 nm. According to the literature the band in the region between 210 nm and 245 nm could be related to the presence of ZrO_2, moreover the band in the region between 260 nm and 380 nm could be related to the presence of CeO_2.[60,61] The UV spectrum of ZrO_2 sample shows one absorption peak at 220 nm. According to Ranga Rao et al.[61] an adsorption band at 245 nm means a predominantly m-ZrO_2 sample. When CeO_2 content
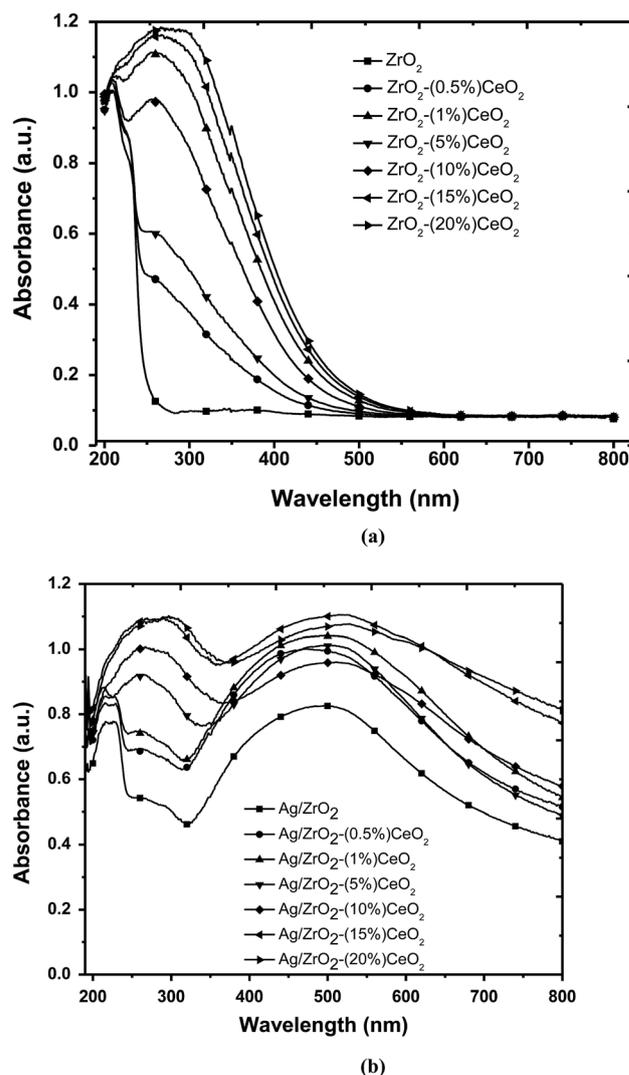
(a)

(b)

Fig. 3 Spectra UV-Vis for (a) ZrO_2, ZrO_2–($X\%$)CeO_2 supports and (b) Ag/ZrO_2, Ag/ZrO_2–($X\%$)CeO_2 catalysts.

Table 2 Crystal size of the ZrO_2 support

Catalysts	Crystal size by Scherrer's equation (nm)	Crystal size by TEM (nm)
ZrO_2	9.7	10
ZrO_2–(5%)CeO_2	9.5	9
ZrO_2–(20%)CeO_2	7.5	6

increase the two intense absorption bands at 220 nm and 260 nm disappear into a very broad band. So it is interesting to note that at higher CeO_2 contents, the bands become very broad with the absorption band of ZrO_2 at 220 nm in the mixed oxides almost disappearing. This latter result is in good agreement with other studies.[53,60,61]

Fig. 3 also contains the spectra for reduced Ag/ZrO_2, and several Ag/ZrO_2–(X%)CeO_2 containing catalysts. It can be seen from this latter figure that in the case of Ag/ZrO_2 catalyst there is the presence of a strong absorption peak around 490 nm in the visible range; on the other hand, for the other Ag/ZrO_2–(X%)CeO_2 samples the strong absorption peak share found between 490 nm and 520 nm, showing that the band position change in each sample with increasing the metal content of ceria. This is characteristic of surface plasmon absorption corresponding to Ag^0 nanoparticles, which illustrate the successful reduction of Ag_2O particles.[28,73] There have been several studies for silver monometallic catalyst supported showing different band position of surface plasmon absorption but in each study with different supports (Table 3). It is important to point out that the most intense plasmon absorption is for the Ag/ZrO_2–(15%)CeO_2. This finding suggests that this catalyst should contain the larger proportion of metallic silver. On other words Ag/ZrO_2–(15%)CeO_2 has more abundance of Ag^0 nanoparticles compared to their monometallic counterparts. This result shows better performance of chemisorption of oxygen over Ag/ZrO_2–(15%)CeO_2 and Ag/ZrO_2–(20%)CeO_2 than the rest of catalyst.[53] For oxidation reactions it is know that oxygen mobility on the catalyst metal surface will enhance the surface reaction and consequently maximize catalytic activity. Moreover, other small peak that appear at 200 nm in monometallic silver supported on ZrO_2–(X%)CeO_2 can be assigned to the Ag^+ ions to the $4d^{10} \rightarrow 4d^9 5s^1$ transition of Ag^+ ions highly dispersed on the support.[28]

TEM measurements were carried out in order to evaluate crystal sizes and morphologies of catalyst on arbitrarily selected areas. The results of HRTEM analysis performed on both support and monometallic catalysts are presented in Fig. 4. According to Fig. 4a, c and e it can be seen that crystal size of ZrO_2 is bigger than mixed oxides. Besides, the smaller crystal size indicates that ZrO_2–(20%)CeO_2 should have a larger total surface area than ZrO_2, in agreement with BET results.[39] Moreover, the crystallographic structure of catalyst was also studied by TEM electron diffraction patterns as can be seen also

on Fig. 4, whereas catalyst supports were of polycrystalline nature and did not show diffraction pattern of a cubic phase.[62–64] Easily detectable agglomerated particles have been observed on ZrO_2–(5%)CeO_2 and ZrO_2–(20%)CeO_2, while on ZrO_2 it is hardly notice the presence of agglomerated particles. Quinelato et al.[41] has shown that because of the particles aggregation, the surface area could be hardly detected when it is measured by physisorption N_2.

On the other hand, Fig. 4b, d and f show the micrographs of fresh and reduced Ag/ZrO_2, Ag/ZrO_2–(5%)CeO_2, Ag/ZrO_2–(20%)CeO_2 catalysts respectively. In each case the mean particle size of silver crystal were 9 nm, 12 nm and 4 nm respectively. These results showed that crystal particles were slightly bigger than when determined by H_2 chemisorption.[21] Interestingly and confirming previous results, the smallest particle size was found in the sample with the highest ceria metal content. The absence of the presence of metallic silver can be explained by the strong metal–support interaction effect or either the solubilization of the silver into the support.[64]

The ZrO_2, ZrO_2–(20%)CeO_2, Ag/ZrO_2 and Ag/ZrO_2–(20%)CeO_2 supports and catalysts were further analyzed with X-ray Photoelectron Spectra (XPS) to verify the surface composition and oxidation states of the surface elements. The oxidation states of Ce, Ag, Zr were analyzed by fitting the curves of Zr_{3d}, Ce_{3d}, O_{1s}, Ag_{3d}. Table 4 shows different values of binding energies (BEs) according to analyzed metal sample. The binding energies were determined using the C 1s at 285 eV as standard in the analysis.

XPS spectra of Zr_{3d} core electrons for calcined supports ZrO_2, ZrO_2–(20%)CeO_2 and fresh reduced catalyst Ag/ZrO_2, Ag/ZrO_2–(20%)CeO_2 are shown in Fig. 5. As seen in this figure, the Zr_{3d} line profile can be satisfactorily fitted to two doublets whose components are $Zr_{3d\ 5/2}$ and $Zr_{3d\ 3/2}$. The $Zr_{3d\ 5/2}$ feature is located near 182.2 eV and the $Zr_{3d\ 3/2}$ feature is located near 184.6 eV for almost catalysts and supports. ZrO_2 has reported BEs ranging from 181.8 to 182.3 eV. The $Zr_{3d\ 5/2}$ binding energies was in a good agreement with the known data for ZrO_2(IV).[50,65–68]

Fig. 6 shows XPS of $Ce_{3d\ 5/2}$ and $Ce_{3d\ 3/2}$ core levels for calcined and H_2 – reduced samples. According to the literature reports,[69–71] the $Ce_{3d\ 5/2}$ and $Ce_{3d\ 3/2}$ has multiplet signals being fingerprints characterizing Ce^{4+} and Ce^{3+} oxides, respectively. Compared with these data reported in the literature, we observed Ce^{4+} feature in the ZrO_2–(20%)CeO_2 and Ag/ZrO_2–(20%)CeO_2, while two weak signals from the presence of Ce^{3+} appeared at 903 eV and 885 eV. Accordingly, the ZrO_2–(20%)CeO_2 support and Ag/ZrO_2–(20%)CeO_2 catalyst containing both Ce(IV) and Ce(III) species.[58,59] Damyanova et al.[50] studied Pt catalysts supported on pure ZrO_2 and CeO_2–ZrO_2 mixed oxides with different CeO_2 content through XPS. In the case of Pt/CeO_2, they found the $Ce_{3d\ 5/2}$ was 882.8 eV, which was characteristic of CeO_2 but in the case of the catalysts containing 1–12 wt% CeO_2 were ranging from 882.2 to 882.4 eV which were characteristic of CeO_2(IV) and Ce_2O_3(III). Galtayries et al.[67] studied CeO_2 and CeO_2–ZrO_2 mixed oxides with 15, 50, 68 and 80 wt% CeO_2 through XPS. They reported % Ce^{4+} for CeO_2 of 70% and for CeO_2–ZrO_2 mixed oxides with 15, 50, 68 and 80 wt% CeO_2 of

Table 3 Surface plasmon adsorption of different silver supported catalysts

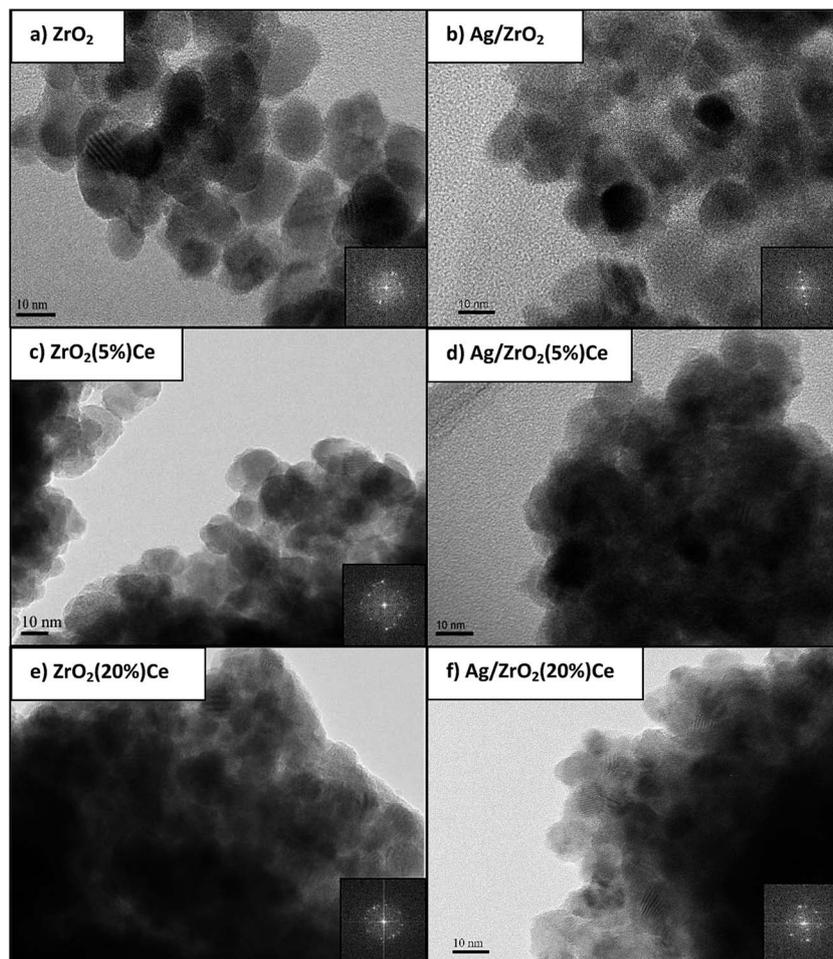| Catalyst	Adsorption range (nm)	Reference
Ag/TiO_2 nanocomposites	445	Haibin et al.[73] 2008
2.2% Ag/TiO_2	480	Sandoval et al.[81] 2011
Ag/Al_2O_3	425	Zhang et al.[23] 2008
$Ag/BaCO_3$	390	Zheng et al.[63] 2012
4.5% $Ag/SBA-15$	385	Zheng et al.[78] 2013
Ag/TiO_2	416	Zhang et al.[82] 2006
Ag/SiO_2	408	Mamontov et al.[25] 2011

Fig. 4 TEM images for ZrO_2, ZrO_2–$(X\%)CeO_2$ supports and Ag/ZrO_2, Ag/ZrO_2–$(X\%)CeO_2$ catalysts.

Table 4 Binding energies obtained from the XPS studies (eV)

Catalysts	$Ag_{3d\ 5/2}$	O_{1s}	$Ce_{3d\ 5/2}$	$Zr_{3d\ 5/2}$	$Zr_{3d\ 3/2}$
ZrO_2	—	530.1, 531.5, 532.5	—	182.2	184.6
ZrO_2–$(20\%)CeO_2$	—	530.0, 531.4, 532.6	882.9	182.2	184.6
Ag/ZrO_2	368.2	529.9, 531.2, 532.1	—	182	184.4
Ag/ZrO_2–$(20\%)CeO_2$	368.5	530.0, 531.3, 532.3	882.6	182.2	184.6

between 57 and 63%. In this latter study the BEs of $Ce_{3d\ 5/2}$ for CeO_2–ZrO_2 mixed oxides (882.1 eV, 882 eV, 882.1 eV, 881.8 eV) were slightly smaller than CeO_2. According to them this slightly negative shift of BEs was attributed that cerium is mainly in the Ce^{4+} oxidation state, with a certain increase in the Ce^{3+}. For the samples prepared in our study, the $Ce_{3d\ 5/2}$ of Ag/ZrO_2–(20%) CeO_2 is 0.3 eV smaller than of ZrO_2–$(20\%)CeO_2$, indicating mayor abundance of Ce^{3+} species, after doping of silver. Der-ekaya et al.[72] attributed the value Ce_{3d} peak of 882.6 eV for the presence of Ce(III).

Fig. 7 shows the Ag_{3d} region consisted of 2 peaks which correspond to $Ag_{3d\ 5/2}$ and $Ag_{3d\ 3/2}$. The $Ag_{3d\ 5/2}$ binding energies of Ag/ZrO_2 and Ag/ZrO_2–$(20\%)CeO_2$ were 368.2 eV and 368.5 eV respectively. These results demonstrate that only one form of Ag is present, in the form of Ag^0. This is because we did

not observe any peak corresponding to the oxidized silver species located around 367.7 eV. The $Ag_{3d\ 5/2}$ of our samples can be compared with values were ranging from 368.1 to 368.5 eV for metallic silver and 367.6–367.8 eV for Ag_2O.[68,73–79] Thus, it is concluded from the XPS measurements that the majority of the silver ions in the nanoparticle synthesis are reduced and are in the metallic form or zero valent state for all prepared samples. Besides, there is an another important observation referred to BEs of $Ag_{3d\ 5/2}$ of our samples. For the Ag/ZrO_2–$(20\%)CeO_2$, the BE of $Ag_{3d\ 5/2}$ is 386.5 eV, which is slightly bigger than Ag/ZrO_2, which is 368.2 eV. Wang et al.[77] studied the binding energy shift of Ag and Au supported on MCM, TiO_2 and Al_2O_3. They attributed such a slightly shift to the possible electron transfer from the support to the particles. Zheng et al.[78] attributed the slightly shift in Au_{4f} BE value,
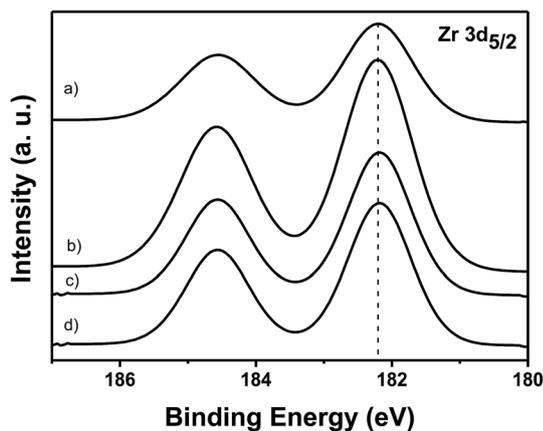
Fig. 5 XPS Zr 3d spectra for (a) ZrO_2–(20%)CeO_2, (b) ZrO_2 supports and (c) Ag/ZrO_2–(20%)CeO_2, (d) Ag/ZrO_2 catalysts.
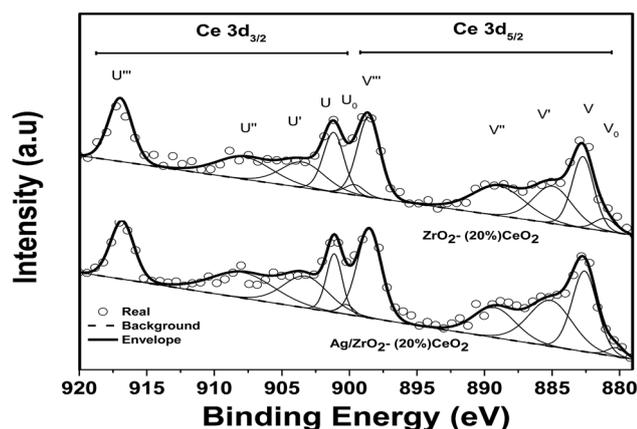

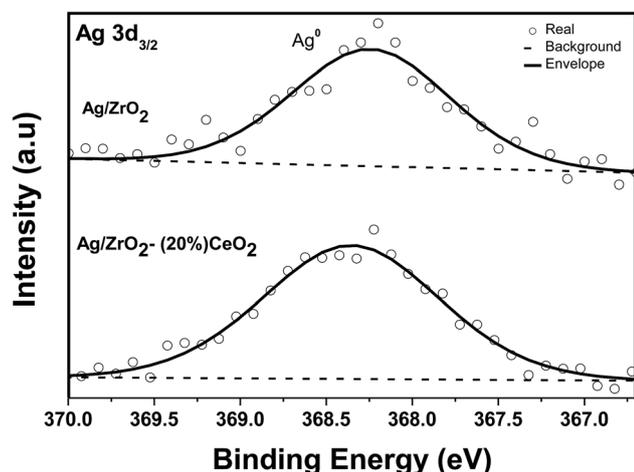**Fig. 6** XPS Ce 3d spectra for ZrO_2–(20%)CeO_2 support and Ag/ZrO_2–(20%)CeO_2 catalyst.

Fig. 7 XPS Ag 3d spectra for support Ag/ZrO_2 and Ag/ZrO_2–(20%)CeO_2 catalyst.

observed between Au/SBA-15 (BE = 83.7 eV) and bulk metallic Au (BE = 84 eV) to the interaction between support and Au nanoparticles.

Hence, based on the above reports, we propose that Ag in ZrO_2 and ZrO_2–(20%)CeO_2 are of a metallic nature, and 0.3 eV difference in $Ag_{3d\ 5/2}$ we observed between those catalysts and bulk metallic silver is due to the interaction between support and Ag nanoparticles. A similar observation was already made by other investigators for the Ag and Au nanoparticles but they assigned the size and shape of metal nanoparticles are also responsible for the binding energy shift.[77,79] In the case of most transition metals, upon oxidation, the observed core-levels BEs shift toward higher energies, and the positive BE shifts increase as the oxidation state increases. However, silver is one of the few examples of lowered binding energy in the oxidized state. Another discussion point implies that through Ag supported on ZrO_2–(20%)CeO_2 mixed oxides, the silver has a greater tendency to win electrons.[74,77,78] This phenomenon may suggest the interaction between Ce and Ag as: $Ag^+ + Ce^{4+} \rightarrow Ag^0 + Ce^{3+}$. There was a little positive shift between this binding energy because in the case of Ag/ZrO_2–(20%)CeO_2 the binding energy is higher than Ag/ZrO_2 as a result of electron transfer from the support to the particle. In other words, as a result to the partial reduction of CeO_2 to CeO_{2-x} the presence of CeO_2 promotes changes in the chemical environment of silver, which it is favorable for more atoms of Ag to stay in a metallic state during the hydrogen pretreatment step. In addition, partial electron transfer from CeO_2 to Ag_2O may occur, leading to an increase in the d-electron density of the surface silver atoms, which improve the catalyst performance.

XPS, UV-Vis spectrometry and TEM confirms that when ceria is present in high concentration enhance strong metal–support interaction effect.

Activity tests

Results from Fig. 8 show that the maximum activity for silver monometallic catalyst was Ag/ZrO_2–(15%)CeO_2. This behavior can be related to several factors such as: strong metal–support interaction, high dispersion and support reducibility that influence the release of more surface oxygen atoms during the reaction. On Ag/ZrO_2–CeO_2 catalysts with 5, 10, 15 and 20% ceria the MTBE conversion has values between 52 and 90%, being the Ag/ZrO_2–(15%)CeO_2 catalyst the most active with 90% MTBE conversion. This latter catalyst had also the highest metallic dispersion. It can be concluded that there is a relationship between the crystal size of support and the metallic dispersion of silver that lead an improved catalytic performance. On the other hand, the complete catalytic oxidation of MTBE yields CO_2 and H_2O as final products. However, if the mineralization is not totally completed some intermediates can be formed. This latter phenomenon produces issues in the efficient of the process. The reaction pathway of MTBE catalytic oxidation has been extensively reported in the literature[15,16] where different compounds such as methanol, isopropyl alcohol, *tert*-butyl alcohol and acetone have been identified as intermediates products of the MTBE catalytic oxidation reaction. The intermediate identified in the present work was acetone.
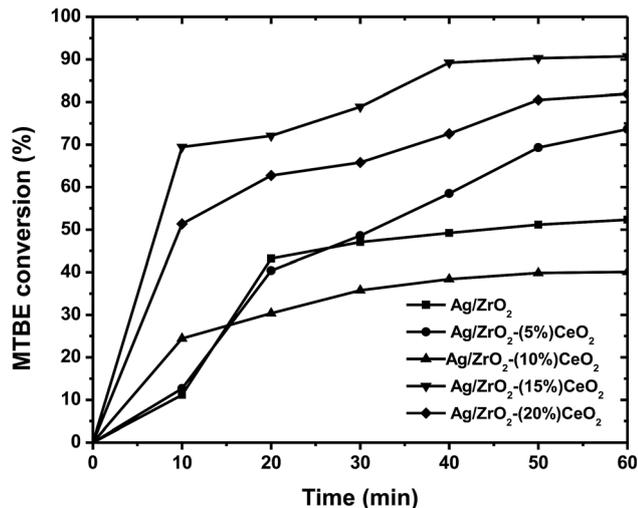
Fig. 8   MTBE conversions as a function of the time for silver supported catalysts.

Fig. 9   TOC abatement as a function of the time for silver supported catalysts.

According to the results in Table 5 it is possible to analyze that in a TOC conversion between 69 and 80% and in a conversion of MTBE between 82 and 90% there is no presence of acetone, this lead to infer that there is a possible catalytic oxidation almost complete for silver catalysts supported with higher content of ceria.

In TOC conversion for monometallic catalysts (Fig. 9) it is strongly distinguished the effect of ceria dopant on the conversion of intermediates, because at a high content of cerium oxide (15 to 20%) it results in high percentages of TOC conversion (69 and 80%), so the reaction rate is faster for the conversion of intermediates and therefore, the concentration of the intermediate compounds is degraded more efficiently. According to the reported by Cervantes et al.[16] this latter result is controlled by the relative abundance of Ce^{4+}.

It is generally accepted that the oxidation reactions over mixed oxide catalyst proceed according to the redox model proposed by Mars and van Krevelen.[83] Based on their findings, the following reactions are proposed to explain the effect of the partial reduction of ceria on metallic silver:

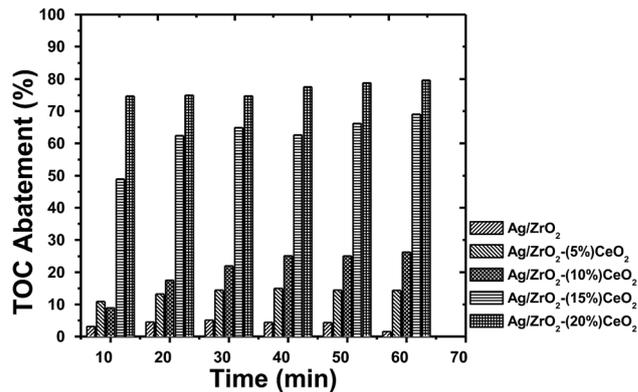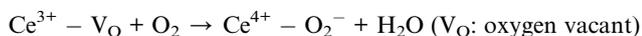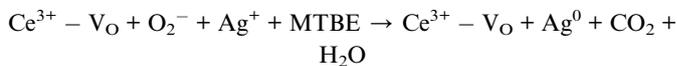(1) Oxygen is adsorbed in oxygen vacant site over ceria surface lattice.

$$Ce^{3+} - V_O + O_2 \rightarrow Ce^{4+} - O_2^- + H_2O \ (V_O: \text{oxygen vacant})$$

(2) The partial reduction of ceria is reversible because of oxygen adsorbed in oxygen vacancy as a result Ag^0 becomes Ag^+.

$$Ag^0 + Ce^{4+} - O_2^- \rightarrow Ce^{3+} - V_O + O_2^- + Ag^+$$

(3) Ag^+ attack MTBE for the conversion to $CO_2 + H_2O$.

$$Ce^{3+} - V_O + O_2^- + Ag^+ + MTBE \rightarrow Ce^{3+} - V_O + Ag^0 + CO_2 + H_2O$$

It is known that oxygen vacancies of zirconia–ceria support play an important role in the dispersion of silver. These oxygen vacancies are the result of anionic deficiencies that reduce Ce^{4+} to Ce^{3+}. Then, this process of self-reduction can be accelerated by the addition of silver that attacks the weak ceria surface oxygen bond allowing their release from the support lattice. Decreasing the zirconia–ceria support crystal size leads to the formation of higher number of surface oxygen and therefore a higher number of metallic silver active sites. Furthermore, the ratio between the crystal size and oxygen vacancies can influence the amount of silver atoms that can be deposited on the support. Greater metal dispersion was found at higher ceria content (i.e. 15 and 20%) because the total oxygen vacancies of the catalyst support depend on ceria loading.[80] The oxygen vacancies are acid sites called Lewis sites where a nucleophilic

Table 5   Activity and selectivity for the catalyst wet-air oxidation of MTBE after 60 min of reaction. MTBE conversion (X_C), TOC abatement (X_{TOC}) and intermediate concentration (acetone) as a function of the time for silver supported catalysts

Catalysts	$X_C{}^a$ (%)	$X_{TOC}{}^a$ (%)	A^a (mmol l^{-1})	$r_1{}^a$ (mmol h^{-1} g$_{met}{}^{-1}$)	Selectivity to $CO_2{}^a$
Ag/ZrO$_2$	52	10	24	1560	19
Ag/ZrO$_2$–(5%)CeO$_2$	73	14	4	2190	19
Ag/ZrO$_2$–(10%)CeO$_2$	40	26	4	1200	65
Ag/ZrO$_2$–(15%)CeO$_2$	90	69	n.d.	2700	77
Ag/ZrO$_2$–(20%)CeO$_2$	82	80	n.d.	2400	98

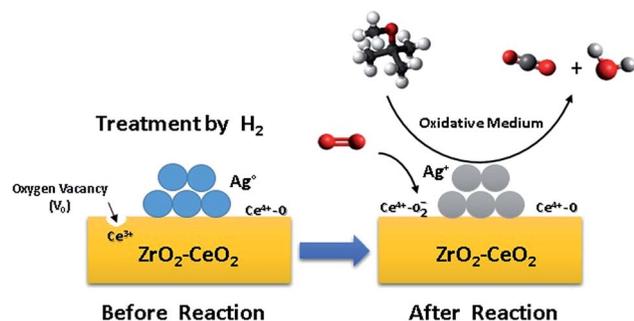^{a} Obtained after 1 h of reaction n.d. = not detected.

Fig. 10 Scheme proposed to explain the effect of the partial reduction of ceria on metallic silver to destroy MTBE by CWAO.

substrate can be deposited. During the oxidation reaction it is known that superoxide species (O^{2-}) are formed on a partially reduced CeO_2 surface as a result of the present of free electrons.[21]

Small crystal size of zirconia–ceria support interacts with Ag more strongly, so that the reactivity of catalyst was enhanced (Fig. 10).

Conclusions

From the study it can be concluded by the use of the deposition–precipitation method it is possible the homogeneous incorporation of low amount of Ag to the tetragonal ZrO_2–CeO_2 and monoclinic–tetragonal ZrO_2 lattice. It was also found that CeO_2 is a structural promoter for silver on ZrO_2 because it can improve the dispersion of silver on the catalyst support and possibly inhibit the sintering of silver during the reaction. On the other hand, zirconia tetragonal phase (t-ZrO_2) stability was also enhanced by CeO_2 addition, meanwhile its mean crystallite size was diminished according to DRX and TEM results. CeO_2 is an electronic promoter for silver over ZrO_2 as it can chance the chemical environment by preventing silver to oxidize due to an increase the d-electron density of the surface silver atoms. These results were confirmed for the monometallic catalyst with the highest ceria content.

Through XPS, UV-Vis spectrometry and TEM should be clearly seen that the highest ceria content promotes strong metal support interaction.

Indeed, small zirconia crystal size produce high silver metal dispersion because of the electron transfer from ceria in the lattice of zirconia to silver and as a collateral effect the improvement in the effectiveness of MTBE oxidation catalytic reaction. As a result, ZrO_2–CeO_2 is an active support and can enhance the activity of MTBE catalytic wet air oxidation. Catalyst Ag/ZrO_2–(15%)CeO_2 was the most active catalyst in the conversion of MTBE with 90%. However, TOC conversion reached 80% for the catalyst Ag/ZrO_2–(20%)CeO_2, presenting a higher selectivity to CO_2 with 98%, therefore is the most active for CWAO reaction of MTBE mineralizing intermediaries in a more efficient way.

References

1 G. Li, T. An, J. Chen, G. Sheng, J. Fu, F. Chen, S. Zhang and H. Zhao, *J. Hazard. Mater.*, 2006, **138**, 392–400.
2 A. Rossner and D. R. U. Knappe, *Water Res.*, 2008, **42**, 2287–2299.
3 J. M. Britto, S. B. de Oliveira, D. Rabelo and M. do C. Rangel, *Catal. Today*, 2008, **133–135**, 582–587.
4 M. F. Dignac, P. Ginestet, D. Rybacki, A. Bruchet, V. Urbain and P. Scribe, *Water Res.*, 2000, **34**, 4185–4194.
5 Q. Li, C. Kang and C. Zhang, *Process Biochem.*, 2005, **40**, 873–877.
6 M. van Afferden, K. Z. Rahman, P. Mosig, C. De Biase, M. Thullner, S. E. Oswald and R. A. Müller, *Water Res.*, 2011, **45**, 5053–5074.
7 J. C. Campos, R. M. H. Borges, A. M. Oliveira Filho, R. Nobrega and G. L. Sant'Anna, *Water Res.*, 2002, **36**, 95–104.
8 D. P. Lince, L. R. Wilson and G. A. Carlson, *Bull. Environ. Contam. Toxicol.*, 1998, **61**, 484–488.
9 L. Toran, C. Lipka, A. Baehr, T. Reilly and R. Baker, *Water Res.*, 2003, **37**, 3756–3766.
10 T. C. Schmidt, S. B. Haderlein, R. Pfister and R. Forster, *Water Res.*, 2004, **38**, 1520–1529.
11 A. Kolb and W. Püttmann, *Water Res.*, 2006, **40**, 3551–3558.
12 A. Safarzahed-Amiri, *Water Res.*, 2001, **35**, 3706–3714.
13 J. Sutherland, C. Adams and J. Kekobad, *Water Res.*, 2004, **38**, 193–205.
14 I.-P. Chen, S.-S. Lin, C.-H. Wang, L. Chang and J.-S. Chang, *Appl. Catal., B*, 2004, **50**, 49–58.
15 I. Cuauhtémoc, G. Del Angel, G. Torres, J. Navarrete, C. Angeles-Chavez and J. M. Padilla, *J. Ceram. Process. Res.*, 2009, **10**, 512–520.
16 A. Cervantes, G. Del Angel, G. Torres, G. Lafaye, J. Barbier Jr, J. N. Beltramini, J. G. Cabañas-Moreno and A. Espinoza de los Monteros, *Catal. Today*, 2013, **212**, 2–9.
17 U. Hübner, U. von Gunten and M. Jekel, *Water Res.*, 2015, **68**, 150–170.
18 J. Barbier Jr, F. Delano, F. Jabouille, D. Duprez, G. Blanchard and P. Isnardd, *J. Catal.*, 1998, **177**, 378–385.
19 J. Gaálováa, J. Barbier Jr and S. Rossignol, *J. Hazard. Mater.*, 2010, **181**, 633–639.
20 Q. Liu, Y. Cao, W.-L. Dai and J.-F. Deng, *Catal. Lett.*, 1998, **55**, 87–91.
21 Lj. Kundakovic and M. Flytzani-Stephanopoulos, *Appl. Catal., A*, 1999, **183**, 35–51.

22 D. Chen, Z. Qu, S. Shen, X. Li, Y. Shi, Y. Wang, Q. Fu and J. Wu, *Catal. Today*, 2011, **175**, 338–345.

23 R. Zhang and S. Kaliaguine, *Appl. Catal., B*, 2008, **78**, 275–287.

24 Z. Qu, M. Cheng, W. Huang and X. Bao, *J. Catal.*, 2005, **229**, 446–458.

25 G. V. Mamontov, T. I. Izaak, O. V. Magaev, A. S. Knyazev and O. V. Vodyankina, *Russ. J. Phys. Chem. A*, 2011, **85**, 1540–1545.

26 T. Nanba, S. Masukawa, A. Abe, J. Uchisawa and A. Obuchi, *Appl. Catal., B*, 2012, **123–124**, 351–356.

27 Lj. Kundakovic and M. Flytzani-Stephanopoulos, *J. Catal.*, 1998, **179**, 203–221.

28 M. Nolan, S. C. Parker and G. W. Watson, *Surf. Sci.*, 2005, **595**, 223–232.

29 S. P. Badwal, D. Fini, F. T. Ciacchi, C. Munnings, J. A. Kimpton and J. Drennan, *J. Mater. Chem. A*, 2013, **1**, 10768–10782.

30 Y. Kang, M. Sun and A. Li, *Catal. Lett.*, 2012, **142**, 1498–1504.

31 N. Shehata, K. Meehan, M. Hudait and N. Jain, *J. Nanopart. Res.*, 2012, **14**, 1–10.

32 J. A. Montoya, E. Romero-Pascual, C. Gimon, P. Del Angel and A. Monzón, *Catal. Today*, 2000, **63**, 71–85.

33 S. S. Lin, D. J. Chang, C.-H. Wang and C. C. Chen, *Water Res.*, 2003, **37**, 793–800.

34 R. Hyun-Seog, W. Yong and D. L. King, *Top. Catal.*, 2008, **49**, 32–37.

35 D. Weng, J. Li, X. Wu and Z. Si, *J. Environ. Sci.*, 2011, **23**, 145–150.

36 P. López, G. Mondragón-Galicia, M. E. Espinosa-Pesqueira, D. Mendoza-Anaya, Ma. E. Fernández, A. Gómez-Cortés, J. Bonifacio, G. Martínez-Barrera and R. Pérez-Hernández, *Int. J. Hydrogen Energy*, 2012, **37**, 9018–9027.

37 A. V. González, X. Karatzas and L. J. Pettersson, *Fuel*, 2013, **107**, 162–169.

38 X.-R. Chen, Y.-H. Ju and C.-Y. Mou, *J. Phys. Chem. C*, 2007, **111**, 18731–18737.

39 F. Menegazzo, P. Burti, M. Signoretto, M. Manzoli, S. Vankova, F. Boccuzzi, F. Pinna and G. Strukul, *J. Catal.*, 2008, **257**, 369–381.

40 L. Meng, L. Liu, X. Zi, H. Dai, Z. Zhao, X. Wang and H. He, *Front. Environ. Sci. Eng. China*, 2010, **4**, 164–171.

41 A. L. Quinelato, E. Longo, E. R. Leite, M. I. B. Bernardi and J. A. Varela, *J. Mater. Sci.*, 2001, **36**, 3825–3830.

42 R. M. Navarro, M. C. Álvarez-Galván, F. Rosa and J. L. G. Fierro, *Appl. Catal., A*, 2006, **297**, 60–72.

43 V. Dhanala, S. K. Maity and D. Shee, *RSC Adv.*, 2015, **5**, 52522–52532.

44 J. Mikulova, J. Barbier Jr, S. Rossignol, D. Mesnard, D. Duprez and C. Kappenstein, *J. Catal.*, 2007, **251**, 172–181.

45 K.-i. Shimizu, H. Kawachi, K. S.-i. Komai, K. Yoshida, Y. Sasaki and A. Satsuma, *Catal. Today*, 2011, **175**, 93–99.

46 N. A. Saidina Amin and C. M. Chong, *Chem. Eng. J.*, 2005, **113**, 13–25.

47 W. Khaodee, N. Tangchupong, B. Jongsomjit, P. Praserthdam and S. Assabumrungrat, *Catal. Commun.*, 2009, **10**, 494–501.

48 J. A. Montoya, E. Romero-Pascual, C. Gimon, P. Del Angel and A. Monzón, *Catal. Today*, 2000, **63**, 71–85.

49 V. Raju, S. Jaenicke and G.-K. Chuah, *Appl. Catal., B*, 2009, **91**, 92–100.

50 S. Damyanova, B. Pawelec, K. Arishtirova, M. V. Martinez Huerta and J. L. G. Fierro, *Appl. Catal., B*, 2009, **89**, 149–159.

51 R. Pérez-Hernández, A. Gutiérrez-Martínez, J. Palacios, M. Vega-Hernández and V. Rodríguez-Lugo, *Int. J. Hydrogen Energy*, 2011, **36**, 6601–6608.

52 V. Solinas, E. Rombi, I. Ferino, M. G. Cutrufello, G. Colón and J. A. Navío, *J. Mol. Catal. A: Chem.*, 2003, **204–205**, 629–635.

53 G. Postole, B. Chowdhury, B. Karmakar, K. Pinki, J. Banerji and A. Auroux, *J. Catal.*, 2010, **269**, 110–121.

54 C. F. Oliveira, F. A. C. Garcia, D. R. Araujo, J. L. Macedo, S. C. L. Dias and J. A. Dias, *Appl. Catal., A*, 2012, **413–414**, 292–300.

55 S. Xu and X. Wang, *Fuel*, 2005, **84**, 563–567.

56 J. Guo, Z. Shi, D. Wu, H. Yin, M. Gong and Y. Chen, *Mater. Res. Bull.*, 2013, **48**, 495–503.

57 D. Mukherjee, B. G. Rao and B. M. Reddy, *Appl. Catal., B*, 2016, **197**, 105–115.

58 L. Zhang, L. Pan, C. Ni, T. Sun, S. Zhao, S. Wang, A. Wang and Y. Hu, *Int. J. Hydrogen Energy*, 2013, **38**, 4397–4406.

59 Z. Si, D. Weng, X. Wu, Z. Ma, J. Ma and R. Ran, *Catal. Today*, 2013, **201**, 122–130.

60 Q. Yu, X. Wu, X. Yao, B. Liu, F. Gao, J. Wang and L. Dong, *Catal. Commun.*, 2011, **12**, 1311–1317.

61 G. Ranga Rao and B. Gopal Mishra, *Bull. Catal. Soc. India*, 2003, **2**, 122–134.

62 A. Franceschetti, S. J. Pennycook and S. T. Pantelides, *Chem. Phys. Lett.*, 2003, **374**, 471–475.

63 X. Zheng, Q. Zhang, Y. Guo, W. Zhan, Y. Guo, Y. Wang and G. Lu, *J. Mol. Catal. A: Chem.*, 2012, **357**, 106–111.

64 M. Vicario, J. Llorca, M. Boaro, C. Leitenburg and A. Trovarelli, *J. Rare Earths*, 2009, **27**, 196–203.

65 J. Lin, H. Y. Chen, L. Chen, K. L. Tan and H. C. Zeng, *Appl. Surf. Sci.*, 1996, **103**, 307–314.

66 S. D. Jones, L. M. Neal, M. L. Everett, G. B. Hoflund and H. E. Hagelin-Weaver, *Appl. Surf. Sci.*, 2010, **256**, 7345–7353.

67 A. Galtayries, R. Sporken, J. Riga, G. Blanchard and R. Caudano, *J. Electron Spectrosc. Relat. Phenom.*, 1998, **88–91**, 951–956.

68 J. F. Moulder, W. W. Stickle, P. E. Sobol and K. D. Bomber, *Handbook of X-ray photoelectron spectroscopy*, ed. J. Chastain, Perkin Elmer, Eden Praine, U.S.A, 1978.

69 E. Abi-aad, R. Bechara, J. Grimblot and A. Aboukaïs, *Chem. Mater.*, 1993, **5**, 793–797.

70 N. Liu, Z. Yuan, C. Wang, S. Wang, C. Zhang and S. Wang, *Fuel Process. Technol.*, 2008, **89**, 574–581.

71 R. Ran, J. Fan and D. Weng, *Prog. Nat. Sci.: Mater. Int.*, 2012, **22**, 7–14.

72 F. B. Derekaya and C. Güldür, *Int. J. Hydrogen Energy*, 2010, **35**, 2247–2261.

73 H. Li, X. Duan, G. Liu and X. Liu, *J. Mater. Sci.*, 2008, **43**, 1669–1676.

74 P. Sangpour, O. Akhavan and A. Z. Moshfegh, *J. Alloys Compd.*, 2009, **486**, 22–28.

75 X.-Y. Gao, S.-Y. Wang, J. Li, Y.-X. Zheng, R.-J. Zhang, P. Zhou, Y.-M. Yang and L.-Y. Chen, *Thin Solid Films*, 2004, **455–456**, 438–442.

76 A. Zielinska-Jurek, E. Kowalska, J. W. Sobczak, W. Lisowski, B. Ohtani and A. Zaleska, *Appl. Catal., B*, 2011, **101**, 504–514.

77 A.-Q. Wang, J.-H. Liu, S. D. Lin, T.-S. Lin and C.-Y. Mou, *J. Catal.*, 2005, **233**, 186–197.

78 J. Zheng, H. Lin, Y.-n. Wang, X. Zheng, X. Duan and Y. Yuan, *J. Catal.*, 2013, **297**, 110–118.

79 X. Huang, X. Wang, X. Wang, X. Wang, M. Tan, W. Ding and X. Lu, *J. Catal.*, 2013, **301**, 217–226.

80 H. C. Yao and Y. F. Yu Yao, *J. Catal.*, 1984, **86**, 254–265.

81 A. Sandoval, A. Aguilar, C. Louis, A. Traverse and R. Zanella, *J. Catal.*, 2011, **281**, 40–49.

82 L. Zhang, D. Xia and Q. Shen, *J. Nanopart. Res.*, 2006, **8**, 23–28.

83 P. Mars and D. W. van Krevelen, *Chem. Eng. Sci.*, 1954, **3**, 41.